arXiv:2402.04365v4 [physics.ins-det] 10 Apr 2024

A method to observe field-region oxide charge and inter-electrode isolation from CV-characteristics of n-on-p devices

T. Abdilov[a], N. Akchurin[a], C. Carty[a], Y. Kazhykarim[a], V. Kuryatkov[b], T. Peltola[a,*], A. Wade[c]

[a]Department of Physics and Astronomy, Texas Tech University, 1200 Memorial Circle, Lubbock, Texas, U.S.A.
[b]Nanotech Center, Texas Tech University, 902 Boston Ave, Lubbock, Texas, U.S.A.
[c]Department of Physics, Florida State University, 77 Chieftan Way, Tallahassee, Florida, U.S.A.

Abstract

N-on-p silicon sensors will be utilized in the Compact Muon Solenoid (CMS) detector's tracker and High Granularity Calorimeter (HGCAL) in the High Luminosity upgrade of the Large Hadron Collider (HL-LHC). Among their several advantages in terms of radiation hardness over the traditional p-on-n sensors in the extreme radiation environment of the HL-LHC are electron collection instead of holes and overlapping maxima of weighting and electric fields at the charge-collecting electrodes. The disadvantage of the multi-channel SiO$_2$-passivated n-on-p sensors is the generation of an inversion layer under the Si/SiO$_2$-interface by a positive interface-oxide-charge (N_{ox}) that at high densities can compromise the position resolution by creating a conduction channel between the electrodes. This issue is typically addressed by including additional isolation implants (p-stop, p-spray) between n^+-electrodes. Focusing on the guard-ring regions of n-on-p sensors where no isolation implants are applied between the electrodes, a capacitance-voltage (CV) characterization study of both 6-inch wafer test diodes and 8-inch HGCAL prototype and pre-series sensors showed a distinct threshold voltage ($V_{\mathrm{th,iso}}$) in the CV-characteristics of a biased n^+-electrode when its enclosing guard-ring was left floating. When reproduced by simulations, the measured $V_{\mathrm{th,iso}}$ was found to contain information on the field-region N_{ox} and indicate the threshold where the two electrodes become electrically isolated by the influence of the reverse bias voltage. Together with previous studies on the inter-electrode isolation of irradiated n-on-p sensors, the results indicate that position sensitive n-on-p sensors without isolation implants may be feasible in future HEP experiments.

---

[*] Corresponding author
Email address: `timo.peltola@ttu.edu` (T. Peltola)

1. Introduction

In order to cope with the extreme radiation environments of the Large Hadron Collider and future hadron colliders like FCC-hh[1] and SPPC[2], one extensively studied approach to improve the radiation hardness of planar silicon particle detectors is the application of $n^+/p^-/p^+$ (n-on-p, n-in-p) structures instead of the conventional p-on-n configuration [1, 2]. Since radiation introduces acceptor-like bulk defects, no type inversion occurs in the p-type bulk resulting in a favorable combination of the maxima of the weighting and electric fields after irradiation, which maximizes the signal and charge carrier velocity in the vicinity of the collecting electrode [3]. The readout at n^+-electrodes results in a signal generated by the drift of electrons, and since electrons have about three times higher mobility and longer trapping times than holes, the amount of trapped charge carriers during their drift is reduced. This enables a high-speed readout and higher collected charge in n-on-p devices than in conventional sensors. Also, after irradiation the electric fields at the n^+-electrodes are lower than in p-on-n sensors, resulting in better noise performance [1, 4]. Another asset of the n-on-p sensor is the reduced dependence of the charge collection on the reverse annealing of the effective space charge in highly irradiated detectors [5, 6]. As a consequence, n-on-p sensors are the baseline technology for the detector upgrades in, for example, the Compact Muon Solenoid (CMS) experiment's tracker and High Granularity Calorimeter (HGCAL) [7], where the replacement of the endcap calorimeter will involve about 600 m^2 of 8-inch silicon modules [8, 9] that will need to sustain fluences of about 1×10^{16} $\mathrm{n_{eq}cm^{-2}}$[3] and doses in excess of 1.5 MGy.

The disadvantage of n-on-p devices is the more complex fabrication technology due to the required isolation structures between the n^+-electrodes. For example, conventional AC-coupled, poly-Si biased, p-on-n sensors can be processed with 6–7 lithography mask levels, while n-on-p devices require two more lithography steps and additional ion implantations [2]. The isolation implants are utilized to counter the effect from the inherent positive charge that is introduced by impurities during the growth process of $\mathrm{SiO_2}$ inside the oxide and at the Si/$\mathrm{SiO_2}$-interface (N_{ox}). The positive N_{ox} attracts electrons (minority carriers in p-type bulk) from the Si-bulk that form an inversion layer under the interface which acts as a conduction channel between the segmented n^+-electrodes. Radiation induced accumulation of surface damage can lead to a substantial increase of net N_{ox} [10]. The negative space charge of the additional highly p-doped implant between the n^+-electrodes breaks the inversion layer by suppressing the electron density at the vicinity of Si/SiO$_2$-interface, thus preserving the inter-electrode isolation and position resolution. Two solutions for the isolation implants are commonly utilized; p-stop and p-spray (or the combination of the two, 'moderated' p-spray [3]), with localized and uniformly distributed doping concentrations, respectively, along the surface in the inter-electrode gap [11, 12, 13, 14, 15, 16, 17]. For stable device performance, careful tuning of the processing parameters is needed, since high doping concentrations in the isolation implants ($\gtrsim 5 \times 10^{16}$ cm^{-3}) increase the probability of discharges or avalanche effects due to excessive localized electric fields [4, 17, 18]. For the same reason the actual contact between the isolation and n^+ implants should also be avoided [3].

---

[1] Future Circular Hadron Collider

[2] Super Proton-Proton Collider

[3] 1-MeV neutron equivalent fluence

However, previous studies have reported high levels of inter-electrode isolation in n-on-p microstrip sensors without isolation implants before and after irradiations with protons [19, 20] and neutrons [20]. Thus, to investigate further possibilities of planar n-on-p sensor configurations, this study focuses on the properties of the regions of n-on-p devices without isolation implants between n^+-electrodes, i.e., the region between a diode and its guard-ring, and the observed threshold voltage of inter-electrode isolation ($V_{\text{th,iso}}$). $V_{\text{th,iso}}$ introduced in this paper is the threshold voltage where the applied reverse bias voltage becomes sufficiently high to sweep electrons from the inter-electrode gap to the positively biased n$^+$-electrode to the extent that breaks the conduction channel and electrically isolates the electrodes. Simultaneous to this, $V_{\text{th,iso}}$ provides information on the level of N_{ox} in the field-region of an n-on-p sensor.

Two substantially different device types were included in the study: test diodes from a 6-inch HGCAL prototype wafer and the guard-ring periphery region of hexagonal 8-inch HGCAL multi-channel sensors. An accompanying study [10] discusses the mechanisms behind the beneficial impact on inter-electrode isolation introduced by irradiation.

The paper is arranged by first introducing the test-structure samples from 6-inch wafers and the 8-inch HGCAL-prototype and pre-series sensors in Section 2. Next, the measurement and simulation setups are described in Section 3. The experimental and simulated CV-characterization results start in Section 4.1 with the observations and interpretation of $V_{\text{th,iso}}$ in the test-diode $C^{-2}V$-curves, and the investigation of its relation to the oxide charge density at the Si/SiO$_2$-interface (N_{ox}), active thickness of the sensor (t) and Si-bulk doping (N_{B}), as well as the correlation of $V_{\text{th,iso}}$ to the inter-electrode isolation of n^+-electrodes without isolation implants. The results of 8-inch HGCAL sensors are presented in Section 4.2 by first determining the field-region N_{ox} for the various sensor t and configurations, followed by the investigation of $V_{\text{th,iso}}$ of inter-electrode isolation with N_{ox}. Finally, the results are discussed in Section 5, while summary and conclusions are given in Section 6.

2. Test-structure samples and HGCAL sensors

The three 'half-moon' samples in the study with 'Large', 'Half' and 'Quarter' test-diodes and MOS[4]-capacitors (with active areas of 4.0×4.0, 2.5×2.5 and 1.25×1.25 mm^2, respectively) were diced from a 6-inch Hamamatsu Photonics K.K. (HPK) 320-µm-thick n-on-p sensor-wafer[5]. The test structures on the samples in Figure 1a were designed at Institut für Hochenergiephysik (HEPHY). The standard-diffusion process was utilized in the heavily doped backplane blocking contact to produce 300-µm active thickness test diodes. More extensive details of the test-diode design and bulk properties are given in [21].

The HGCAL version 2 prototype (or 'proto-A') and pre-series[6] 8-inch multi-channel n-on-p sensors[7], designed at Fermi National Accelerator Laboratory (FNAL) and produced by HPK, included in the study are presented in Figure 2. The low-density (LD) sensors included both 300- and 200-µm thicknesses, which were produced from physically thinned p-type float zone silicon wafers, resulting in essentially equal active and physical thicknesses. The high-density (HD) sensors with an active thickness of 120 µm were produced by growing epitaxial silicon on a lower resistivity substrate, resulting in a total physical thickness of 300 µm [7]. The n^+-electrodes of the several hundred sensor cells (= channels) displayed in Figure 2 are isolated from each other by 'common' p-stop implants, i.e., one p-stop divides the inter-cell gap (as opposed to 'individual' p-stop where each cell has a dedicated p-stop). Corresponding 'Quarter' MOS-capacitors from the 8-inch sensor wafers in Figure 1b designed at HEPHY were also included in the electrical characterization investigation.

Both the test structures and the HGCAL sensors have $\langle 100 \rangle$ crystal orientation, and about 700-nm-thick silicon dioxide (SiO_2) as the passivation layer with inherent positive oxide charge. The gap between the n^+-implant of the test diode and its guard-ring implant is 100 µm for all three test-diode sizes, while the periphery region of the HGCAL sensors is presented in Figure 3.

3. Measurement and simulation setups

For the electrical characterizations of both the test structures and the multi-channel HGCAL sensors, two measurement setups were utilized at Texas Tech University (TTU). The capacitance-voltage (CV) characterizations of the test structures were carried out with a single-channel custom probe station. The reverse

---

[4] Metal-Oxide-Semiconductor

[5] Early prototype wafer for the HGCAL.

[6] Consecutive advanced HPK production stages towards the final HGCAL sensor production parameters.

[7] For shortness, the prototypes will be referred to as 'HGCAL sensors' in the following sections.

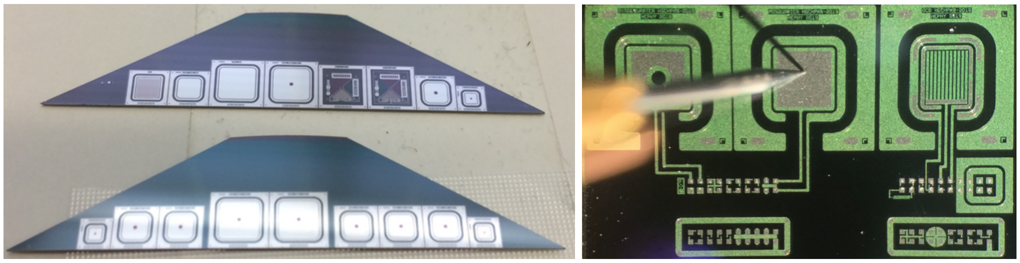

(a)

(b)

Figure 1: Test structure samples. (a) ‘Half-moon’ samples with test structures diced from a 6-inch wafer [21]. Top: three test diodes, two MOS-capacitors (second and third from left) and other test structures. Bottom: nine test diodes. (b) Close-up of a test-structure sample diced from an 8-inch HGCAL wafer with the MOS-capacitor connected to the measurement circuit by a probe needle. A test diode enclosed by its guard-ring is visible on the left-side of the MOS-capacitor.

bias voltage of the test diode (or the gate voltage of the MOS-capacitor) was supplied by a Keithley 2410 source measure unit (SMU) while the capacitance was read out by a Keysight E4980AL LCR-meter. The negative high voltage ($-$HV) was provided to the backplane of the test structure by a vacuum chuck, and the connection to the measurement circuit was realized with a probe needle on the segmented front surface, as shown in Figure 1b. A second probe needle was applied for the grounding of the test-diode’s guard-ring. The setup is described in detail in refs. [10, 21].

The corresponding CV-characterizations of the HGCAL sensors were carried out with a multi-channel setup utilizing an automated ARRAY dual-card setup [23] that enables the electrical characterizations of the 8-inch sensors containing several hundred individual cells. For the connection to the measurement circuit a dedicated probe card for each sensor type in Figure 2 was required. Probe cards for full sensors in Figures 2a and 2b and for HD-partial sensor in Figure 2c utilized front-side and back-side biasing, respectively. The guard-ring next to the HV-ring in Figure 3 is left floating in all probe-card types. The remote control and data acquisition functions were realized with a LabVIEW™-based custom program (HexDAQ version 1.7[8]). The same SMU and LCR-meter units were used for both single-channel and multi-channel circuit measurements.

The 2D device-simulations were carried out using the Synopsys Sentaurus[9] finite-element Technology

---

[8] https://gitlab.cern.ch/CLICdp/HGCAL/

[9] http://www.synopsys.com

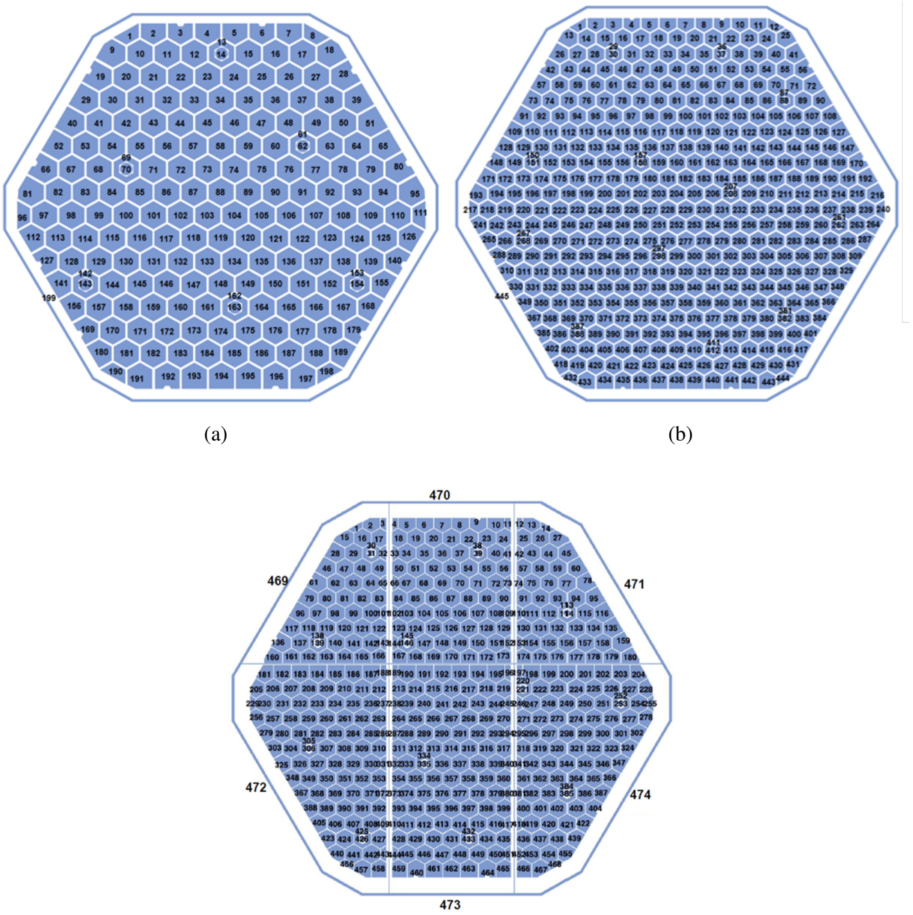

(a)

(b)

(c)

Figure 2: HGCAL 8-inch multi-channel sensor designs included in the study. (a) Full low-density (LD) float-zone Si-sensor with 198 channels (pre-series). (b) Full high-density (HD) epitaxial Si-sensor with 444 channels (pre-series). The cell area of the HD sensors is less than half of the area of the LD-sensor cells to control the cell capacitance. (c) Multi-Geometry Wafer (MGW) HD epitaxial Si-sensor (version 2 prototype). Boundary of the 'bottom-cut' partial sensor with 288 channels is shown by the horizontal blue line in the middle part of the sensor. The channels of the full sensors are enclosed by a single biased guard-ring (channels 199 and 445 in Figures 2a and 2b, respectively), while the channels of the 'bottom-cut' partial HD-sensor are divided into three regions by three biased guard-rings (channels 472, 473 and 474 in Figure 2c).

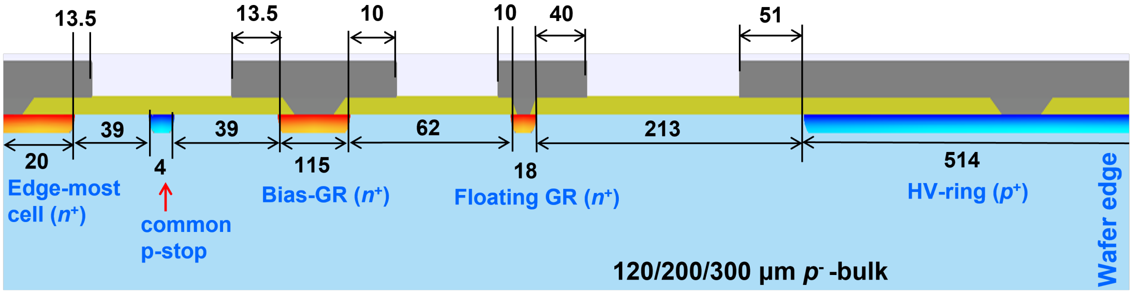

Figure 3: Cross-sectional sketch of the front-side of the periphery region of an HGCAL sensor. The horizontal dimensions are in µm. Gray: 1-µm-thick Al-layer for DC-coupled electrical contacts, dark yellow: 700-nm-thick SiO_2 layer. The backplane of the sensor has the p^+-blocking contact with 1-µm-thick uniform Al-layer. The biased guard-ring (bias-GR) is grounded during the measurements of the cells of the multi-channel sensor, while the high voltage (HV)-ring is used for the front-side biasing scheme [22], where the applied $-$HV connects to the backplane via the low-resistivity edge-region under the HV-ring (with a $p^+/p^-/p^+$ configuration).

Computer-Aided Design (TCAD) software framework. For the test-diode and MOS-capacitor simulations, a structure consisting of a DC-coupled n^+-pad between two n^+ guard-rings (GR) (either grounded or floating), and a metal-oxide-silicon structure, respectively, were implemented. The backplane doping profile and oxide thickness were set to match the real test structures as described in Section 2 and in [21].

For the HGCAL sensor simulations of the three active thicknesses, the periphery-region with the dimensions displayed in Figure 3 was implemented. Results from spreading resistance profiling (SRP) measurements of the sensors carried out within the HGCAL community were used as an input for the doping profiles, shown in Figure 4. The bulk-doping (N_B) levels were extracted from the CV-measured full-depletion voltages (V_{fd}) of the sensor-cells shown in Appendix A and implemented in the simulation.

4. Experimental and simulation results

4.1. 6-inch wafer test structures

The room-temperature CV-characterizations of the test structures were carried out at a frequency of 200 kHz to control the dissipation factor and stabilize the measurements (reduced capacitive impedance [24]) of the low-capacitance test diodes with a minimum capacitance of 0.54 pF (‘Quarter’ diode).

The measured CV-characteristics of the ‘Large’ MOS-capacitor and test diode are presented in Figure 5. The flat band voltage (V_{fb}) of the MOS-capacitor was determined by the flat-band-capacitance method (C_{fb}

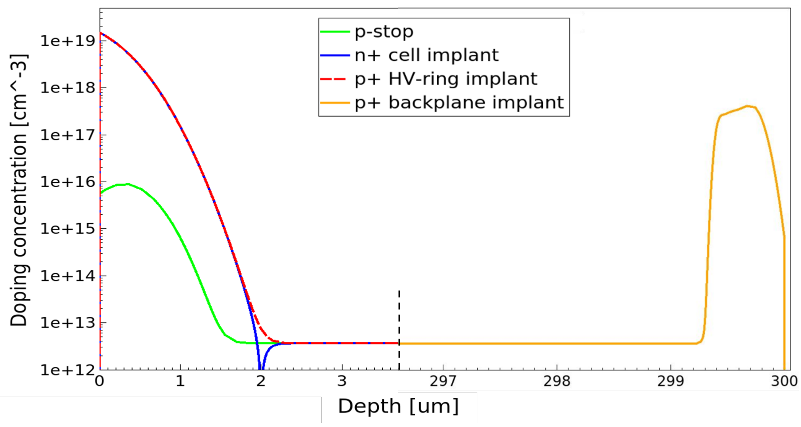

Figure 4: Input doping profiles for the 300-µm-thick HGCAL LD-sensor periphery-region TCAD-simulation. Identical front-side (Depth $= 0$ µm) doping profiles were set for the HD-sensors, while the low-resistivity substrate of the epitaxial sensor was modeled by an error function starting from the backplane (Depth $=$ 300 µm) with an abrupt drop to bulk-doping level at 120-µm depth.

in Figure 5a). The extracted $V_{\mathrm{fb}} = -4.28 \pm 0.02$ V was then used to resolve the oxide charge density at the Si/SiO$_2$-interface as $N_{\mathrm{ox}} = (1.08 \pm 0.05) \times 10^{11}$ cm^{-2} [10]. It was also shown in [10] that in the absence of hysteresis whether the CV-sweep of the pre-irradiated MOS-capacitor is initiated from deep accumulation or from deep inversion (-9 V and 0 V in Figure 5a, respectively), the contribution from mobile ionic charges (N_{M}) and interface traps (N_{it}) to N_{ox} is negligible, leading to N_{ox} being described essentially by the fixed oxide charge density (N_{f}), i.e., $N_{\mathrm{ox}} \cong N_{\mathrm{f}}$. As shown in Figure 5a, the measured V_{fb} was reproduced by the simulation with the input value of $N_{\mathrm{ox}} = N_{\mathrm{f}}$ (implemented at the Si/SiO$_2$-interface as a positive charge-sheet with a uniform distribution along the interface) within uncertainty of the experimentally extracted N_{ox} (with contributions to uncertainty from measured V_{fb} and oxide capacitance (C_{ox})). Therefore, this approach is maintained for the field-region N_{ox} simulations on the test diodes and HGCAL sensors (in the following sections the simulation tuning-parameter at the Si/SiO$_2$-interface will be referred to as N_{ox}).

Shown in Figure 5b, the characteristic C_{geom}-values –where capacitance is dependent only on the material and the geometry of the device– and the slopes in the dynamic-region of the measured $C^{-2}V$-curves from either solely the test-diode pad (‘GR grounded’) or both the pad and its guard-ring (‘GR + diode’) reflect the differences in the active areas A involved in the measurements by the relation

$$C_{\mathrm{geom}} = \epsilon_{\mathrm{s}} \frac{A}{d}, \tag{1}$$

where ϵ_s is the product of vacuum permittivity and the relative permittivity of silicon, and d is the active thickness of the device [25]. Hence, the measured capacitances are $C = C_\mathrm{diode}$ and $C' = C_\mathrm{diode} + C_\mathrm{GR} = C_\mathrm{tot}$ for the two configurations throughout the applied voltage range.

However, the measurement with the floating guard-ring (i.e., guard-ring is disconnected from the biasing circuit, thus its potential is 'floating' with changing conditions in the device) in Figure 5b displays a double slope in the dynamic-region of $C^{-2}V$-curve with a distinct threshold voltage ($V_\mathrm{th,iso}$) between the two slopes. The identical slope with C_tot-curve at $V < V_\mathrm{th,iso}$ suggests that the diode and its guard-ring are shorted in this voltage-region. This is caused by the conduction channel between the test-diode pad and the guard-ring –where there is no isolation implant–, formed by the positive oxide charge (Q_ox) of $\mathrm{SiO_2}$ attracting minority carriers, i.e., electrons, from Si-bulk to the Si/$\mathrm{SiO_2}$-interface. As shown by the simulated evolution of the electron density in the vicinity of the interface in Figure 5c, at $V \geq V_\mathrm{th,iso}$ the Coulomb force from the positively biased n^+-pad of the test diode overcomes the attraction from Q_ox, and the electrons are swept from the inter-electrode gap (electron density drops by about nine-orders-of-magnitude from $V < V_\mathrm{th,iso}$) to the n^+-pad, resulting in the test diode becoming isolated from the guard-ring. Due to this process, the area involved in the CV-measurement of the test-diode pad is reduced, which, as a consequence of Eq. 1, is observed as an abrupt decrease of C in Figure 5b, forming a double-slope in the dynamic-region of the CV-curve.

With the approach presented in Appendix A, $V_\mathrm{fd} = 280$ V was extracted from the C_diode-curve in Figure 5b and the derived value of $N_\mathrm{B} = 4.0 \times 10^{12}$ $\mathrm{cm^{-3}}$ (utilizing the relation $N_\mathrm{B} = 2\epsilon_\mathrm{s} V_\mathrm{fd}/(ed^2)$, where e is the elementary charge [25]) was applied as an input to the test-diode simulation. As displayed in Figure 5b, by tuning the input N_ox both the voltage of $V_\mathrm{th,iso}$ and the test-diode CV-characteristics with its guard-ring either grounded or floating can be closely reproduced by the simulation. From further measurements and simulations with varied input N_ox focusing on the CV-curves of a test diode with its guard-ring floating in Figure 6a, it is evident that $V_\mathrm{th,iso}$ is not dependent on V_fd.

In Figure 6b, where $V_\mathrm{th,iso} \approx V_\mathrm{fd} - 85$ V, the influence of the two factors in the evolution of the active volume (involved in the test-diode pad CV-measurement) with reverse bias voltage is visible:

- Isolation between the test-diode pad and the guard-ring.
- The presence or absence of opposing electric field-lines from the guard-ring, corresponding to whether the guard-ring is grounded or floating, respectively.

The sensitivity to $V_\mathrm{th,iso}$ is also visible in the CV-measurement with the guard-ring grounded, as the slight

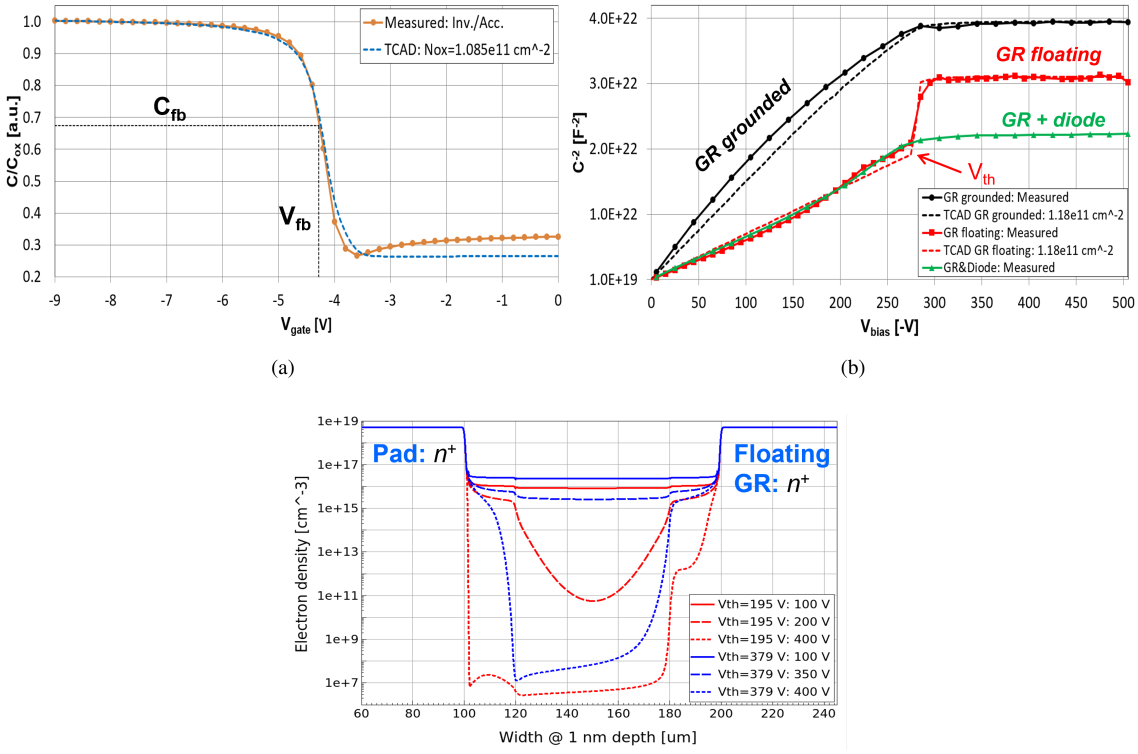

(a)

(b)

(c)

Figure 5: (a) Measured and TCAD-simulated CV-characteristics of a p-bulk MOS-capacitor. Measured CV-curves were identical for the CV-sweeps starting either from inversion (Inv.) or accumulation (Acc.) regions. (b) Measured and simulated CV-characteristics of an n-on-p test diode, with its guard-ring (GR) either grounded, floating or measured together with the test diode (GR + diode). The point of $V_{\text{th,iso}}$ reproduced by the simulation with $N_{\text{ox}} = 1.18 \times 10^{11}$ cm^{-2} is indicated. The measured test structures in (a) and (b) were from the same 6-inch Si-wafer. (c) Simulated evolution of electron density with reverse bias voltage at 1-nm depth from the Si/SiO$_2$-interface and between the test-diode pad and its floating guard-ring. The two values of $V_{\text{th,iso}}$, 195 and 379 V, correspond to N_{ox} values of 1.0×10^{11} and 1.4×10^{11} cm^{-2} in Figure 6a, respectively. The metal-overhang edges of the two electrodes are at 120 and 180 µm, respectively.

non-linearity in the dynamic-region of the $C^{-2}V$-curve vanishes above $V_{\text{th,iso}}$. This suggests that the conduction-channel is also present when the guard-ring is grounded, keeping the test-diode pad and the guard-ring shorted at $V < V_{\text{th,iso}}$, and indicating that $V_{\text{th,iso}}$ is independent of the two CV-measurement configurations in Figure 6b. The opposing field-lines from the grounded guard-ring stop the lateral expansion of the pad's active volume with bias voltage, which mitigates the influence of the shorted electrodes on the $C^{-2}V$-curve at voltages below $V_{\text{th,iso}}$. The same feature is also visible throughout the dynamic-region of the measured $C^{-2}V$-curve with grounded guard-ring in Figure 5b, where $V_{\text{th,iso}}$ is about 5 V below V_{fd}. Additionally, both figures display that the aforementioned feature in the measured CV-characteristics of the test diode with grounded guard-ring is not reproduced by the 2D-simulation. This is likely to be due to the limitation of the cross-sectional 2D-structure to reproduce the subtle effect from the lateral expansion of the guard-ring field lines that confine the active volume of the test-diode pad from its four sides at the voltages where the pad and the guard-ring are still shorted. Thus, due to considerably more pronounced influence from $V_{\text{th,iso}}$ on the CV-characteristics of a test diode with floating guard-ring, the combined experimental and simulation investigation of the correlation between $V_{\text{th,iso}}$ and field-region N_{ox} is focused on this configuration.

Finally, the absence of opposing field-lines from the guard-ring in the CV-measurements of the test diode with floating guard-ring in Figures 5b and 6 enables greater lateral expansion of the active volume of the test-diode pad even when it is isolated from the guard-ring ($V > V_{\text{th,iso}}$), resulting in higher C_{geom} (with $A = A_{\text{diode}} + A_{\text{lateral}}$ in Eq. 1) than the measurement with the guard-ring grounded.

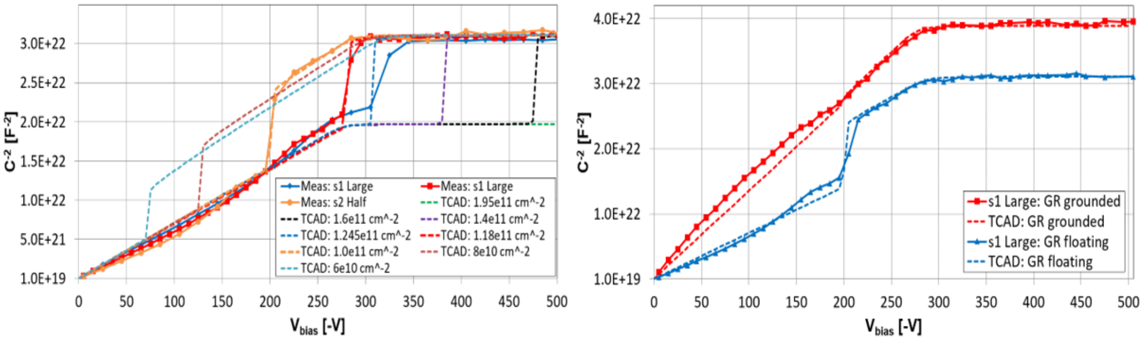

(a)

(b)

Figure 6: Measured and simulated CV-characteristics of 300-µm-thick n-on-p test diodes. 's1'='half-moon' sample one. (a) Influence of N_{ox} on $V_{\text{th,iso}}$ for test diodes with a floating guard-ring. The measured C_{geom} of the 'Half'-diode is scaled to the C_{geom} of the 'Large'-diodes. The three measured values of $V_{\text{th,iso}}$ are reproduced by the simulation with N_{ox}-values of 1.0×10^{11}, 1.18×10^{11} and 1.245×10^{11} cm^{-2}. (b) Results for a test diode with guard-ring grounded or floating and with $V_{\text{th,iso}}(195\text{ V}) < V_{\text{fd}}(280\text{ V})$. The simulation applied $N_{\text{ox}} = 1.0 \times 10^{11}$ cm^{-2}.

With additional simulated data-points Figure 7a displays a power-law dependence between N_{ox} and $V_{\text{th,iso}}$ by the fit $N_{\text{ox}} = 7.67 \times 10^9 |V_{\text{th,iso}}|^{0.488}$ for the 100-µm-width pad-to-guard-ring gap of the measured test diodes. Doubled pad-to-guard-ring gap in Figure 7a shows a weak dependence of $V_{\text{th,iso}}$ on the gap width, which becomes negligible at $N_{\text{ox}} < 1.2 \times 10^{11}$ cm^{-2}. Thus, Figure 7a provides a tool to determine field-region N_{ox} from the measured $V_{\text{th,iso}}$ of the CV-curve of an n-on-p test diode with a floating guard-ring or more generally, in the field-region between two n^+-electrodes with no isolation implant.

Figures 7b and 7c present the measured CV-characteristics of 14 test diodes with guard-ring floating from three 'half-moon' samples diced off from the corners of one 6-inch wafer. As shown in Figure 8, the values of $V_{\text{th,iso}}$ vary between the 'half-moon' samples and with the position on the sample, indicating a non-uniformity of N_{ox} over the 6-inch wafer, while no dependence on the test-diode size is visible. One of the test diodes (sample 1 'Large' in Figure 7b) displays also a significant sensitivity to repeated measurements with $\Delta V_{\text{th,iso}} \approx 100$ V between the first and fourth measurements, after which no change of $V_{\text{th,iso}}$ was observed with further measurements. This could indicate a suppression of electrons pulled to the Si/SiO$_2$-interface by the positive oxide charge, but since repeated measurements on other test diodes showed negligible effect on $V_{\text{th,iso}}$, understanding the nature of this effect is left out of the scope of the following analysis.

Applying the fit from Figure 7a to all measured $V_{\text{th,iso}}$ in Figures 7b and 7c gives for field-region $\overline{N}_{\text{ox}} = (1.10 \pm 0.09) \times 10^{11}$ cm^{-2}, while the measurements of the MOS-capacitors on samples 1 and 2 (sample 3 with nine test-diodes shown in the bottom-part of Figure 1a did not contain any MOS-capacitors) result in gate $\overline{N}_{\text{ox}} = (1.05 \pm 0.09) \times 10^{11}$ cm^{-2}. Thus, the measurement-simulation and direct-measurement approaches to extract the field-region and the gate $\overline{N}_{\text{ox}}$, respectively, are in agreement within uncertainty. Figure 8 displays a comparison between the individual N_{ox}-results extracted from the field-region of the test diodes and from the MOS-capacitor measurements.

The correlation of $V_{\text{th,iso}}$ observed in CV-characteristics to the change in the inter-electrode resistance (R_{int}) for n^+-electrodes without isolation implant is presented in Figure 9a. It is evident that the CV-extracted $V_{\text{th,iso}}$ is identical to the voltage where R_{int} increases abruptly by about ten-orders-of-magnitude, i.e., $V_{\text{th,iso}}(CV) = V_{\text{th,iso}}(R_{\text{int}})$. The simulated change of R_{int} above $V_{\text{th,iso}}$ is also in close agreement with experimental results [20]. Hence, the electron removal from the inter-electrode gap by applied reverse bias voltage in Figures 5c and 9b results in a high level of R_{int} which isolates the n^+-electrodes at a given $V_{\text{th,iso}}$ that can be observed in a CV-measurement. Since in R_{int}-simulation both n^+-electrodes are biased (unlike in CV-simulation where the guard-ring is floating), Figure 9a also displays that $V_{\text{th,iso}}$ is independent of whether one or both of the electrodes are biased. This supports the observation of the measured $C^{-2}V$-curves with either grounded or floating guard-ring in Figure 6b where both configurations show sensitivity to the same $V_{\text{th,iso}}$. Finally, the R_{int}-curve for the highest N_{ox} in Figure 9a shows that for $N_{\text{ox}} < 1.85 \times 10^{11}$ cm^{-2}, n^+-electrodes of a 300-µm-thick n-on-p test diode, i.e., a pad-sensor, remain isolated without an isolation

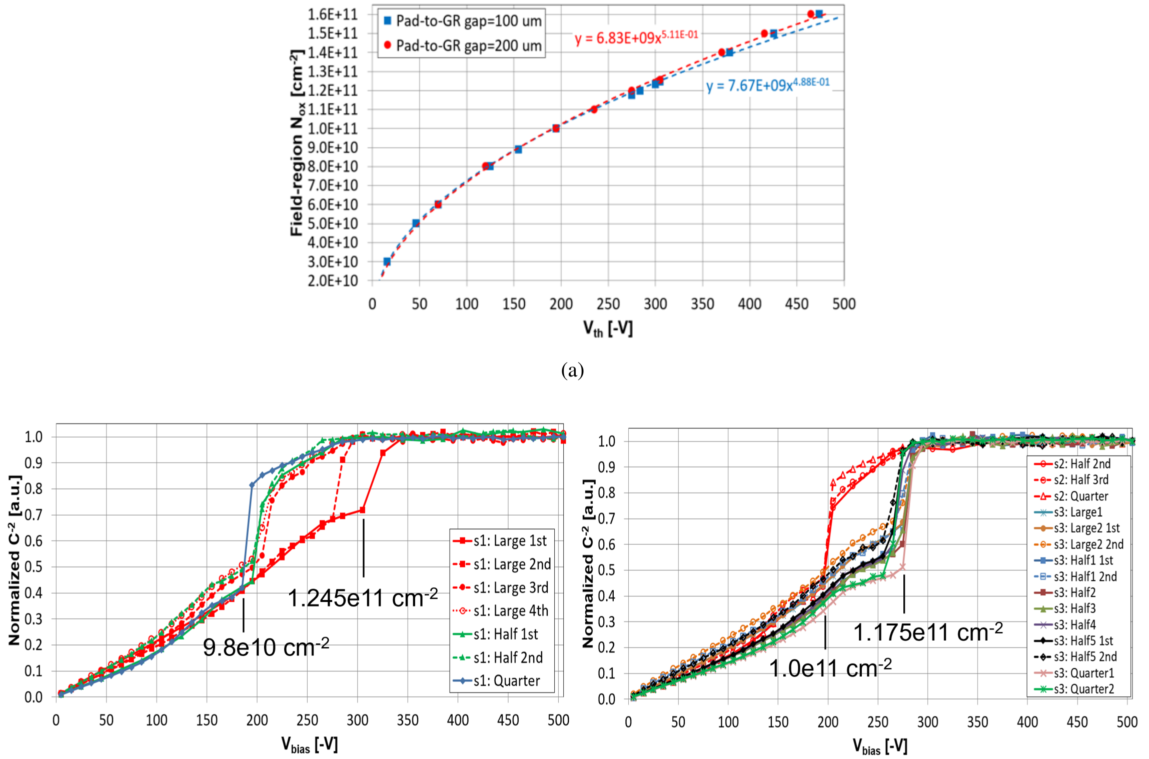

(a)

(b) Sample 1.

(c) Samples 2 and 3.

Figure 7: (a) The simulated dependence of the field-region N_{ox} on $V_{\mathrm{th,iso}}$ in a 300-µm-thick n-on-p test diode for two gap widths between the test-diode pad and its floating guard-ring ('Pad-to-GR gap'). The fit parameters for the two data sets are displayed in the plot. (b) and (c) Measured CV-characteristics of 14 300-µm-thick n-on-p test diodes with guard-ring floating. The three 'half-moon' samples including the test diodes are named as 's1–3', while repeated measurements on a test diode are indicated as '1st–4th'. The extreme values of field-region N_{ox}, extracted fron the simulations utilizing the fit for 100-µm pad-to-GR gap in Figure 7a, are indicated.

implant when operated at the bias voltage of 600 V.

The sensitivity of $V_{\mathrm{th,iso}}$ to the influence of N_{B} and the active thickness (t) of the sensor is presented in Figure 10. With a constant t and N_{ox}, $V_{\mathrm{th,iso}}$ displays a strong dependence on N_{B} in Figure 10a with $V_{\mathrm{th,iso}} > V_{\mathrm{fd}}$ at $N_{\mathrm{B}} \leq 3 \times 10^{12}$ cm^{-3} and $V_{\mathrm{th,iso}} < V_{\mathrm{fd}}$ at $N_{\mathrm{B}} \geq 4 \times 10^{12}$ cm^{-3}. As shown in Figure 10b, increased N_{B} suppresses the minority carrier density close to Si/SiO$_2$-interface leading to reduced voltages required to isolate the electrodes, thus moving $V_{\mathrm{th,iso}}$ to lower voltages in Figure 10a. Additionally, with a constant N_{B} and N_{ox}, $V_{\mathrm{th,iso}}$ displays significant dependence on t in Figure 10c, with $V_{\mathrm{th,iso}} > V_{\mathrm{fd}}$ at $t < 300$ µm and

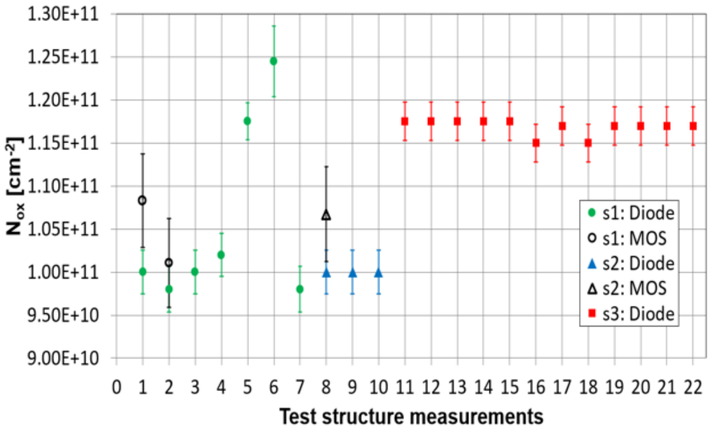

Figure 8: A comparison of the field-region N_{ox} extracted from the test diode $V_{\text{th,iso}}$-values in Figures 7b and 7c between the three 'half-moon' samples, as well as with gate N_{ox} extracted from the V_{fb}-values of the MOS-capacitors on the samples 1 and 2 ('s1–2').

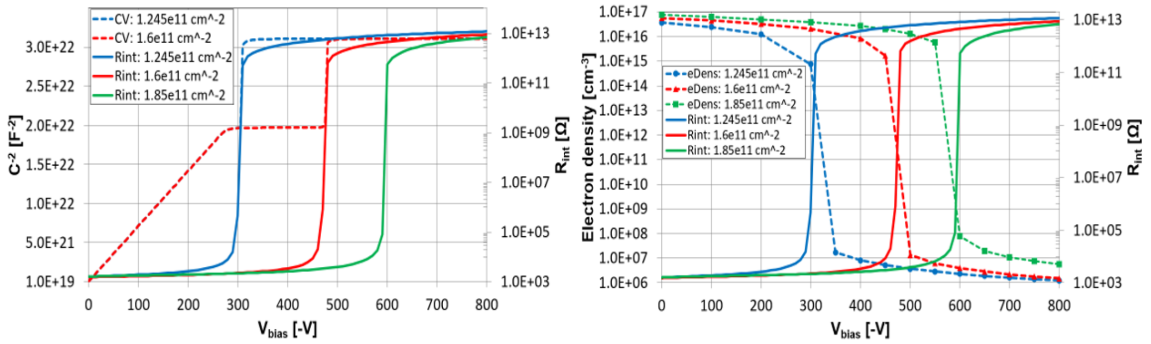

(a)

(b)

Figure 9: Comparison of simulated $V_{\text{th,iso}}$ in the R_{int}-characteristics of a 300-µm-thick n-on-p test diode for two N_{ox}-levels from Figure 6a, along with N_{ox}-level that results in $V_{\text{th,iso}}(R_{\text{int}}) = 600$ V with (a) $V_{\text{th,iso}}$ in the CV-characteristics of the two lower N_{ox}-levels and (b) the change in electron density at 1 nm depth from the Si/SiO$_2$-interface in the middle of the inter-electrode gap.

$\Delta V_{\text{th,iso}} \approx -60$ V when t is reduced from 300 to 120 µm. Since for a given voltage higher electric fields are generated in a thinner sensor, a lower voltage for a thinner sensor is required to generate sufficient field to reduce electron density in the inter-electrode gap to a level that isolates the electrodes, displayed by lower $V_{\text{th,iso}}$ with reduced t in Figure 10c. As a consequence, CV-extracted $V_{\text{th,iso}}(N_{\text{ox}}, N_{\text{B}}, t)$ and therefore the results in Figures 7a and 9a should be considered for fixed $N_\mathrm{B} = 4.0 \times 10^{12}$ cm^{-3} and $t = 300$ µm.

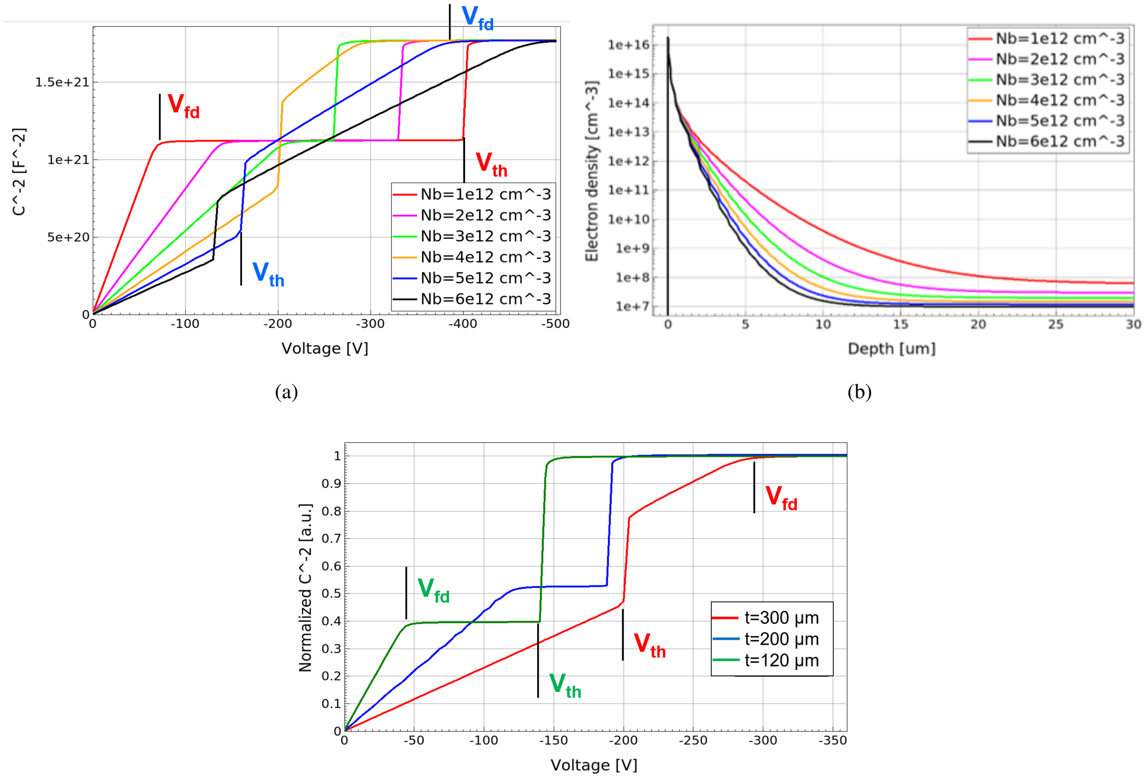

(a)

(b)

(c)

Figure 10: Simulation results of an n-on-p test-diode with floating guard-ring for the influence of N_B and t on $V_\mathrm{th,iso}$. (a) Change of $V_\mathrm{th,iso}$ with N_B for constant $t = 300$ µm and $N_\mathrm{ox} = 1 \times 10^{11}$ cm^{-2}. (b) Corresponding electron density to Figure 10a close to the Si/SiO$_2$-interface at mid-gap between pad and guard-ring for $V = 0$. (c) Change of $V_\mathrm{th,iso}$ with t for constant $N_\mathrm{B} = 4 \times 10^{12}$ cm^{-3} and $N_\mathrm{ox} = 1 \times 10^{11}$ cm^{-2}.

4.2. *8-inch HGCAL sensors*

To extend the investigation presented in Section 4.1 to 8-inch HGCAL sensors, the region between the two guard-rings in the periphery of a HGCAL sensor displayed in Figure 3 was considered. To limit the lateral extension of the active region of the multi-channel sensor toward the physical wafer edge, the guard-ring closer to the HV-ring (‘Floating GR’ in Figure 3) is left floating in the ARRAY setup’s probe card by default. The electrical configuration between the biased (bias-GR) and floating guard-rings in the HGCAL sensor is then identical to the test diode with a floating guard-ring (i.e., no isolation implant between the biased and floating n^+-electrodes). The main difference between the devices comes from their geometry, since instead of a square-shaped pad of the test diode, the biased electrode is now a 115 µm-wide strip with a hexagon shape for the full sensors in Figures 2a and 2b, and polygon and rectangle shapes for the Multi-Geometry Wafer (MGW)-sensor in Figure 2c. Additionally, the gap between the two electrodes is 62 and 100 µm for the HGCAL sensor and test diode, respectively. Thus, despite the differences in the device geometry to the test diodes the CV-characteristics of the HGCAL sensors' bias-GR are expected to provide an observation of $V_{\mathrm{th,iso}}$.

As shown in Figures 11 and 12, bias-GR CV-characteristics of all measured HGCAL sensor types display $V_{\mathrm{th,iso}}$ either below (Figures 11a, 11b and 12b) or above (Figures 11c and 12a) V_{fd} (values of $\overline{V}_{\mathrm{fd}}$ are given in Appendix A). In all cases the n^+-electrodes without p-stop isolation implant become isolated at $V_{\mathrm{th,iso}} \leq$ 100 V, which is significantly below the operating voltage of 600 V considered for HGCAL [7]. The wafer-position dependence of $V_{\mathrm{th,iso}}$ observed in the test-diode results in Figures 7b and 7c is also visible in Figure 12 where the 'bottom-cut' partial sensors have three bias-GRs enclosing three regions of the sensor, as shown in Figure 2c. The different lengths between the rectangular bias-GR at the center of the sensor (channel 473) and the two polygonal bias-GRs adjacent to it (channels 472 and 474) in the 'bottom-cut' sensor are reflected in the different values of C_{geom}, according to Eq. 1.

With the observations from Figure 10, dedicated t and N_{B} were applied to each of the modeled sensor structures to reproduce the measured $V_{\mathrm{th,iso}}$ by simulation. After N_{ox}-tuning the main disagreement between simulation and measurement for 300-µm-thick full sensors in Figure 11a is in the region $V < V_{\mathrm{th,iso}}$, where the lower slope of the simulated $C^{-2}V$-curve indicates a wider lateral expansion of the depletion volume before the biased and floating guard-rings become isolated than in the real sensor. In Figure 11b the disagreement between simulation and measurement for 200-µm-thick full sensors is now in the region $V > V_{\mathrm{th,iso}}$, where the further limited decrease of the active volume involved in the bias-GR CV-measurement at $V > V_{\mathrm{fd}} \approx 115$ V is not reproduced by the simulation. The same trend is visible in Figure 11c for 120-µm-thick full sensors even though $V_{\mathrm{fd}} \approx 31$ V, thus the feature is only dependent on $V_{\mathrm{th,iso}}$ and present only in the bias-GR CV-characteristics of full 200- and 120-µm-thick sensors. The onset of the feature has a dependence on active thickness, being about 20 V lower for 120-µm-thick sensors than for 200-µm thickness, while its interpretation is left out of the scope of this study. The sole significant disagreement between simulation and measurement for the partial 'bottom-cut' 120-µm-thick sensors in Figures 12a and 12b is in the abruptness of the decrease of C immediately after $V_{\mathrm{th,iso}}$, indicating that the electrons are being swept from the inter-electrode

Table 1: Active thicknesses, sensor and passivation oxide types, number of measured sensors, the mean field-region oxide charge densities ($\overline{N}_{\text{ox}}$), number of measured MOS-capacitors and the mean gate oxide charge densities ($\overline{N}_{\text{ox,gate}}$) at the Si/SiO$_2$-interface.

Active thickness [µm]	**Sensor type**	**Oxide type**	**Measured sensors**	$\overline{N}_{\text{ox}}$ [$\times 10^{10}$ cm^{-2}]	**Measured MOS**	$\overline{N}_{\text{ox,gate}}$ [$\times 10^{10}$ cm^{-2}]
300	LD full	C	20	6.74 ± 0.14	6	5.2 ± 0.3
200	LD full	C	5	6.64 ± 0.12		
120	HD full	C	4	6.8 ± 0.2		
120	HD 'bottom-cut'	B	2	6.01 ± 0.14	6	4.5 ± 0.5
120	HD 'bottom-cut'	D	2	5.32 ± 0.17	4	4.2 ± 0.4

gap to the positively biased guard-ring more swiftly in the simulation than in measurement. Considering that the length-ratio of the bias-GRs in the 'bottom-cut' partial and the full sensors is roughly $\frac{1}{6}$, the results suggest that the 2D TCAD-simulation is able to reproduce more closely the measured CV-characteristics of the bias-GRs that enclose a smaller sensor-region. This is also supported by the close agreements between measurements and simulations of test diodes in Section 4.1 with substantially smaller area and less complex geometry to the bias-GRs of HGCAL sensors.

The investigated HGCAL sensors included three oxide-quality types:'C' for the full sensors, and 'B' and 'D' for the partial sensors indicating HPK's oxide candidates with the oxide growth thermally and environmentally varied. By generating additional data-points for each sensor configuration and oxide type, the extracted $\overline{N}_{\text{ox}}$ are presented in Table 1. For full sensors with oxide type 'C' the values of $\overline{N}_{\text{ox}}$ remain within uncertainty for the three thicknesses, while being distinctly higher than $\overline{N}_{\text{ox}}$ of both 'B' and 'D'. Comparison with V_{fb}-extracted $\overline{N}_{\text{ox}}$ ($\overline{N}_{\text{ox,gate}}$) from the MOS-capacitor measured results in Table 1 and Figure 13 shows matching qualitative trend between the oxide types, while the values of $\overline{N}_{\text{ox,gate}}$ remain lower than $\overline{N}_{\text{ox}}$ by a factor 0.77 ± 0.13 (considering average $(6.7 \pm 0.3) \times 10^{10}$ cm^{-2} of the field-region $\overline{N}_{\text{ox}}$-values for type 'C' in Table 1) over the three oxide types. The disagreement between $\overline{N}_{\text{ox,gate}}$ and $\overline{N}_{\text{ox}}$ observed here is in contrast with the observed corresponding agreement between test structures in Section 4.1, which suggests that N_{ox} in the field region between the biased guard-ring and HV-ring of HGCAL sensors is somewhat higher than the gate N_{ox} at their respective MOS-capacitors. Since the oxide-quality types available for this investigation are only a subset of the multitude of oxide type candidates provided by HPK to the HGCAL collaboration, further comparisons between the oxide-quality types are not included in the scope of this study.

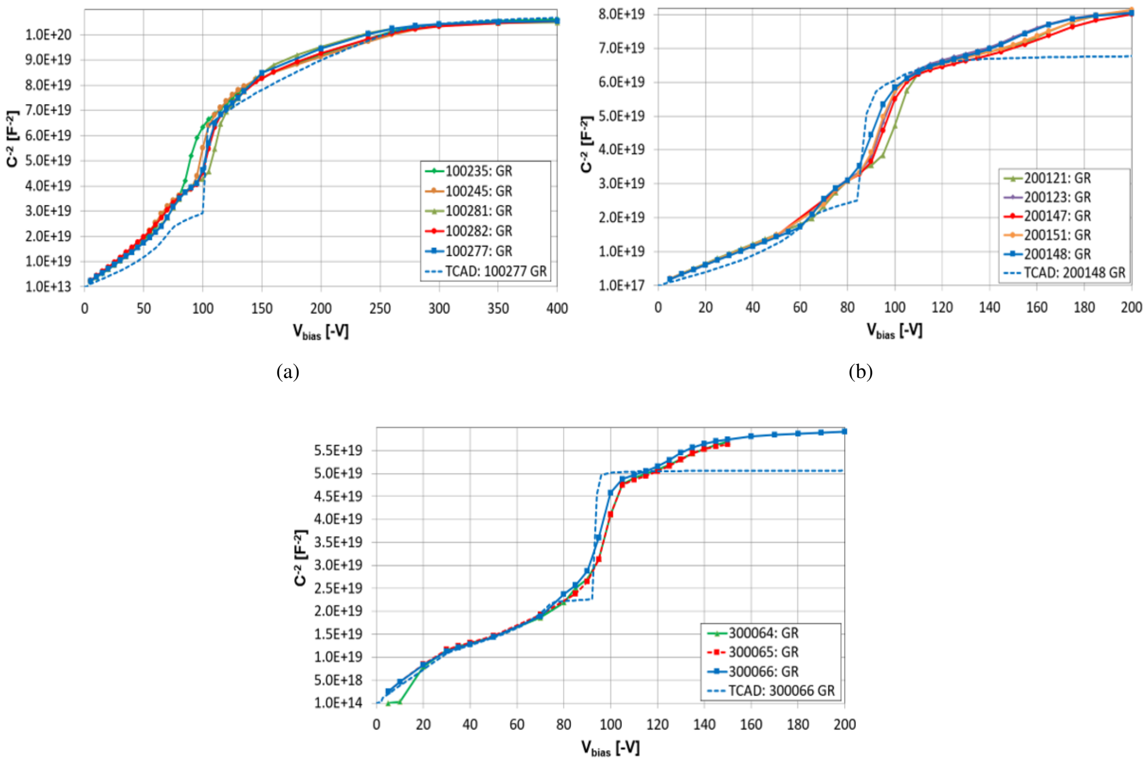

(a)

(b)

(c)

Figure 11: Measured and simulated CV-characteristics for the biased guard-ring ('GR') in full 8-inch HGCAL sensors with oxide type 'C'. Sensor IDs are indicated in the legends, while the simulation input values of N_{B} are given in Figure A.15. (a) Measured results of five 300-µm-thick LD-sensors with $V_{\text{th,iso}}$ of the sensor '100277' reproduced by the simulation with the input $N_{\text{ox}} = 6.90 \times 10^{10}$ cm^{-2}. Out of the 20 measured sensors, only $C^{-2}V$-curves with significant variation in $V_{\text{th,iso}}$ are included in the plot for clarity. (b) Measured results of five 200-µm-thick LD-sensors with $V_{\text{th,iso}}$ of the sensor '200148' reproduced by the simulation with the input $N_{\text{ox}} = 6.45 \times 10^{10}$ cm^{-2}. (c) Measured results of three 120-µm-thick HD-sensors with $V_{\text{th,iso}}$ of the sensor '300066' reproduced by the simulation with the input $N_{\text{ox}} = 6.65 \times 10^{10}$ cm^{-2}.

Displayed in Figure 14a the dependence of the field-region N_{ox} on $V_{\text{th,iso}}$ for the three HGCAL sensor thicknesses (with the simulation input $\overline{N}_{\text{B}}$ from Figures A.15 and A.16) can be described by second-order polynomial fits in the region $N_{\text{ox}} \leq 1.0 \times 10^{11}$ cm^{-2} (a range which includes all extracted $\overline{N}_{\text{ox}}$-values in Table 1). When the simulated $V_{\text{th,iso}}$-range is extended from < 200 V to 600 V, the dependence is best described by linear fits in Figure 14b. The $V_{\text{th,iso}}$-dependence of N_{ox} at both high and low N_{ox}-regions for

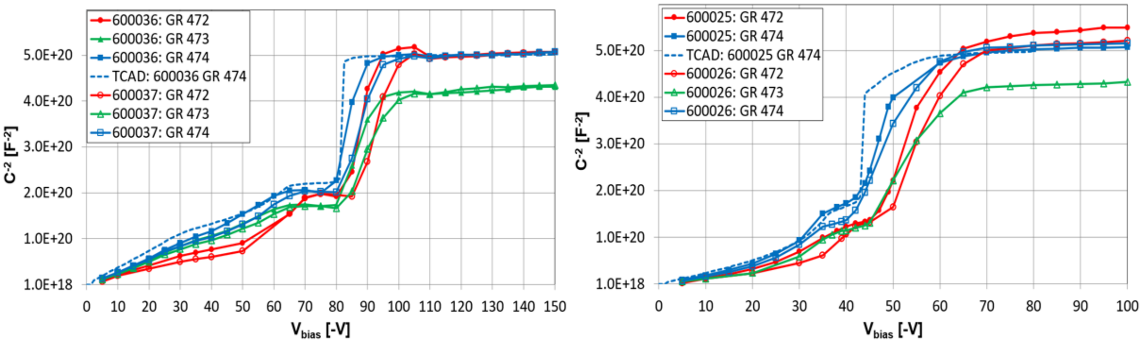

(a) (b)

Figure 12: Measured and simulated CV-characteristics for the biased guard-rings ('GR 472–474'corresponding to the channel numbers in Figure 2c) in 8-inch partial ('bottom-cut') 120-µm HD HGCAL sensors. The simulation input values of N_{B} are given in Figure A.16. (a) Measured results of two sensors with oxide type 'B' with $V_{\mathrm{th,iso}}$ of the 'GR 474' of the sensor '600036' reproduced by the simulation with the input $N_{\mathrm{ox}} = 5.98 \times 10^{10}$ cm^{-2}. (b) Measured results of two sensors with oxide type 'D' with $V_{\mathrm{th,iso}}$ of the 'GR 474' of the sensor '600025' reproduced by the simulation with the input $N_{\mathrm{ox}} = 5.15 \times 10^{10}$ cm^{-2}.

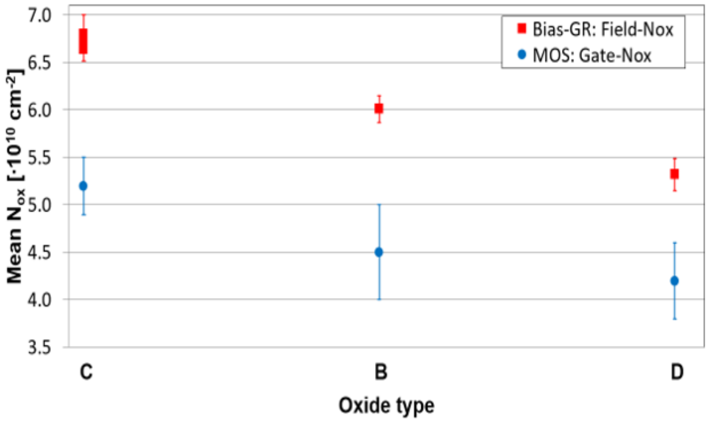

Figure 13: $\overline{N}_{\mathrm{ox}}$-values from Table 1 for the three oxide quality types, extracted either from bias-GR measurements and simulations ('Field-N_{ox}') or from MOS-capacitor measurements ('Gate-N_{ox}').

HGCAL sensors is then distinct from the power-law dependence of the test diodes in Figure 7a, suggesting an influence from the substantially different geometries between the simulated device-structures in Sections 4.1 and 4.2. Since the observed $V_{\mathrm{th,iso}}$ contains simultaneously information on N_{ox} and on the change from low to high levels of R_{int}, shown in Figure 9a, the simulated data-points in Figure 14b provide threshold-values of N_{ox} below which n^{+}-electrodes without isolation implants are predicted to be isolated in HGCAL sensors operated at $V_{\text{bias}} = 600$ V.

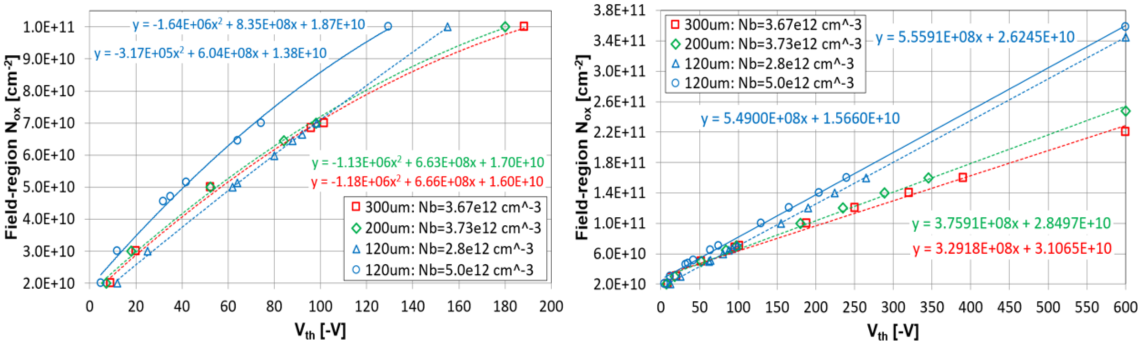

(a) (b)

Figure 14: The simulated dependence of the field-region N_{ox} on $V_{\text{th,iso}}$ for the three active thicknesses of the 8-inch HGCAL sensors with the input values of N_{B} indicated in the legends. (a) Simulation results for the input $N_{\text{ox}} \leq 1.0 \times 10^{11}$ cm^{-2} with second-order polynomial fits to the data-sets. (b) Input N_{ox}-range extended to the levels that result in $V_{\text{th,iso}} = 600$ V with linear fits to the data-sets. The fit parameters are displayed in the plots.

5. Discussion

The results in Section 4.2 indicate that pre-irradiated n-on-p sensors without isolation implants between the channels can reach electrical isolation, and thus uncompromised position resolution between the channels, by the application of sufficient reverse V_{bias} (for the N_{ox}-values in Table 1 at about $V_{\text{bias}} > 40 - 100$ V). As the highest N_{ox}-values in SiO$_2$-passivated Si-sensors with $\langle 100 \rangle$ crystal orientation are typically well below 2×10^{11} cm^{-2} [10, 26], also these levels are expected to be within the isolation range of the operation voltage 600 V, as shown in Figure 14b (for 2×10^{11} cm^{-2} all sensor types become isolated in the range of about 320–500 V).

In irradiated sensors, the surface damage caused by ionizing radiation from charged particles, X-rays or gammas includes the accumulation of N_{f} and deep donor- and acceptor-type N_{it} ($N_{\text{it,don}}$ and $N_{\text{it,acc}}$, respectively) that contribute to the net N_{ox} at the Si/SiO$_2$-interface. Previous experimental R_{int}-results of 200- and 290-µm-thick n-on-p strip-sensors without p-stop implants neutron or proton irradiated to $\Phi =$

6×10^{14} $\mathrm{n_{eq}cm^{-2}}$, corresponding to the estimated Total Ionizing Doses (TID) of 6 and 870 kGy, respectively, show high levels of inter-strip isolation at $V_{\mathrm{bias}} > 100$ V (see Figure 9 in ref. [20]). As described in ref. [10], radiation accumulated levels of $N_{\mathrm{it,don}}$ and $N_{\mathrm{it,acc}}$ comparable to N_{f} introduce a dynamic characteristic to the net N_{ox}, as the fractions of fully occupied N_{it} evolve with applied voltage. Contribution from fully occupied $N_{\mathrm{it,acc}}$ results in considerably low levels of net N_{ox} in the field-region between the positively biased n^+-electrodes (see Figure 8 in ref. [10]) of a position sensitive n-on-p sensor, which remain within the isolation range in Figure 14b. Thus, the radiation-induced accumulation of $N_{\mathrm{it,acc}}$ at the Si/SiO$_2$-interface has a beneficial impact on the inter-electrode isolation in irradiated n-on-p sensors, while simulations [10] and R_{int}-measurements [20] indicate its introduction rate being more prominent in a radiation environment involving hadrons.

Thus, the combined observations before and after irradiation indicate that the inter-electrode isolation and consequently position resolution between n^+-electrodes without isolation implants can be reached and maintained by the application of sufficient V_{bias}, with the tolerance for high net N_{ox}-levels increasing with reduced active thickness of the sensor.

6. Summary and conclusions

Measured CV-characteristics of 6-inch 300-µm-thick n-on-p Si-wafer test diodes with floating guard-ring display a double-slope with a distinct $V_{\mathrm{th,iso}}$ in the dynamic region of $C^{-2}V$-curve. The corresponding TCAD-simulations show that this is due to the electron removal along the Si/SiO$_2$-interface from the inter-electrode gap to the positively biased test-diode pad, until at $V \geq V_{\mathrm{th,iso}}$ the conduction channel between the two n^+-electrodes is broken. This is reflected in the CV-characteristics of the test-diode pad as an abrupt drop of capacitance. The field-region N_{ox} is obtained by tuning its simulation input value until a $V_{\mathrm{th,iso}}$ matching with the measurement is reproduced. The values of N_{ox} determined by this approach agree within uncertainty with N_{ox} extracted from the measured V_{fb} of MOS-capacitors from the same samples. R_{int}-simulations show that the threshold voltage where segmented n^+-electrodes without isolation implants reach high levels of R_{int} and thus become electrically isolated is identical to $V_{\mathrm{th,iso}}(CV)$, i.e., $V_{\mathrm{th,iso}}(CV) = V_{\mathrm{th,iso}}(R_{\mathrm{int}})$. Hence, observation of $V_{\mathrm{th,iso}}(CV)$ provides simultaneously information on both field-region N_{ox} and isolation between n^+-electrodes without isolation implants. Further test-diode simulations show that $V_{\mathrm{th,iso}}$ also has significant dependence on both active thickness and bulk doping of the sensor.

Measured and simulated CV-characteristics of the biased guard-ring on the 8-inch HGCAL-prototype and pre-series sensors with varied Si-bulk and passivation oxide parameters reproduce the observation of

$V_{\text{th,iso}}$ universally. These display low values in the range of about $40 - 100$ V that correspond to field-region $N_{\text{ox}} \approx (5 - 7) \times 10^{10}$ cm^{-2}.

The apparent high isolation levels between n^+-electrodes without isolation implants reachable by the application of sufficient V_{bias} ($<$ 200 V with the initial $N_{\text{ox}} \leq 1 \times 10^{11}$ cm^{-2}) both before and after irradiation in a hadron-dominated radiation environment make this configuration, with a similar number of lithography and ion-implantation steps as p-on-n sensors, a potentially feasible n-on-p sensor candidate for future HEP-experiments. With respect to sensor performance, the isolation implantless configuration of position sensitive n-on-p sensors removes the probability of discharges or avalanche effects due to excessive electric fields at the p-stops.

Acknowledgements

This work has been supported by the US Department of Energy, Office of Science (DE-SC0015592). We thank Ronald Lipton of FNAL for his invaluable insights on the analysis of this investigation. We also thank K. Zinsmeyer, C. Perez, and posthumously P. Cruzan of TTU for their expert technical support.

References

[1] G. Casse, et al., First results on the charge collection properties of segmented detectors made with p-type bulk silicon, Nucl. Instr. & Meth. A 487 (2002) 465–470. `doi:10.1016/S0168-9002(02)00263-2`.

[2] J. Härkönen, et al., Low-temperature TCT characterization of heavily proton irradiated p-type magnetic Czochralski silicon detectors, Nucl. Instr. & Meth. A 583 (2007) 71–76. `doi:10.1016/j.nima.2007.08.198`.

[3] F. Hartmann, Evolution of Silicon Sensor Technology in Particle Physics, 2nd Edition, Springer, 2017. `doi:10.1007/978-3-319-64436-3`.

[4] W. Adam, et al., P-Type Silicon Strip Sensors for the new CMS Tracker at HL-LHC, JINST 12 (2017) P06018. `doi:10.1088/1748-0221/12/06/P06018`.

[5] G. Casse, P. P. Allport, A. Watson, Effects of accelerated annealing on p-type silicon micro-strip detectors after very high doses of proton irradiation, Nucl. Instr. & Meth. A 568 (2006) 46–50. `doi:10.1016/j.nima.2006.05.200`.

[6] G. Kramberger, V. Cindro, I. Mandić, M. Mikuž, M. Zavrtanik, Effective trapping time of electrons and holes in different silicon materials irradiated with neutrons, protons and pions, Nucl. Instr. & Meth. A 481 (2002) 297–305. `doi:10.1016/S0168-9002(01)01263-3`.

[7] CMS Collaboration, The Phase-2 Upgrade of the CMS Endcap Calorimeter, CMS-TDR-019 (Nov. 2017).

[8] E. Brondolin, Silicon sensors for the CMS HGCAL upgrade: challenges, sensor design & electrical characterization, JINST 15 (2020) C05068. `doi:10.1088/1748-0221/15/05/C05068`.

[9] B. Acar, et al., Neutron irradiation and electrical characterisation of the first 8" silicon pad sensor prototypes for the CMS calorimeter endcap upgrade, JINST 18 (2023) P08024. `doi:10.1088/1748-0221/18/08/P08024`.

[10] N. Akchurin, et al., Modeling of surface damage at the Si/SiO$_2$-interface of irradiated MOS-capacitors, JINST 18 (2023) P08001. `doi:10.1088/1748-0221/18/08/P08001`.

[11] J. Kemmer, G. Lutz, Concepts for simplification of strip detector design and production, Nucl. Instr. & Meth. A 326 (1993) 209–213. `doi:10.1016/0168-9002(93)90353-J`.

[12] R. H. Richter, et al., Strip detector design for ATLAS and HERA-B using two-dimensional device simulation, Nucl. Instr. & Meth. A 377 (1996) 412–421. `doi:10.1016/0168-9002(96)00257-4`.

[13] Y. Iwata, et al., Optimal p-stop pattern for the N-side strip isolation of silicon microstrip detectors, IEEE Trans. Nucl. Sci 45 (3) (1998) 303–309. `doi:10.1109/23.682398`.

[14] G. Verzellesi, G.-F. D. Betta, G. Pignatel, Compact modeling of n-side interstrip resistance in p-stop and p-spray isolated double-sided silicon microstrip detectors, in: 2000 IEEE Nuclear Science Symposium, IEEE, Lyon, France, 2000, pp. 25–27. `doi:10.1109/NSSMIC.2000.949004`.

[15] C. Piemonte, Device simulations of isolation techniques for silicon microstrip detectors made on p-type substrates, IEEE Trans. Nucl. Sci NS-53 (3) (2006) 1694–1705. `doi:10.1109/TNS.2006.872500`.

[16] Y. Unno, et al., Evaluation of test structures for the novel n$^+$-in-p pixel and strip sensors for very high radiation environments, Nucl. Instr. & Meth. A 731 (2013) 183–188. `doi:10.1016/j.nima.2013.04.075`.

[17] M. Printz, P-stop isolation study of irradiated n-in-p type silicon strip sensors for harsh radiation environments, Nucl. Instr. & Meth. A 831 (2016) 38–43. `doi:10.1016/j.nima.2016.05.103`.

[18] R. Dalal, et al., Combined effect of bulk and surface damage on strip insulation properties of proton irradiated n^+-p silicon strip sensors, JINST 9 (2014) P04007. `doi:10.1088/1748-0221/9/04/P04007`.

[19] Y. Unno, et al., p-Bulk silicon microstrip sensors and irradiation, Nucl. Instr. & Meth. A 579 (2007) 614–622. `doi:10.1016/j.nima.2007.05.256`.

[20] J-O. Müller-Gosewisch and A. Dierlamm and A. Nürnberg, Influence of surface damage and bulk defects on the interstrip isolation of p-type silicon strip sensors, JINST 16 (2021) P07004. `doi:10.1088/1748-0221/16/07/P07004`.

[21] N. Akchurin, et al., Charge Collection and Electrical Characterization of Neutron Irradiated Silicon Pad Detectors for the CMS High Granularity Calorimeter, JINST 15 (2020) P09031. `doi:10.1088/1748-0221/15/09/P09031`.

[22] M. Baselga, et al., Front-side biasing of n-in-p silicon strip detectors, JINST 13 (2018) P11007. `doi:10.1088/1748-0221/13/11/P11007`.

[23] E. Brondolin, et al., ARRAY: An open source, modular and probe-card based system with integrated switching matrix for characterisation of large area silicon pad sensors, Nucl. Instr. & Meth. A 940 (2019) 168–173. `doi:10.1016/j.nima.2019.06.007`.

[24] L. Stauffer, Fundamentals of semiconductor C-V measurements, EE-Evaluation Engineering 47 (2008) 1–4, Gale Academic OneFile.

[25] S. M. Sze, Physics of Semiconductor Devices, 2nd Edition, John Wiley & Sons, Hoboken New Jersey U.S.A., 1981.

[26] T. Peltola, V. Eremin, E. Verbitskaya, J. Härkönen, Simulation study of signal formation in position sensitive planar p-on-n silicon detectors after short range charge injection, JINST 12 (2017) P09032. `doi:10.1088/1748-0221/12/09/P09032`.

Appendix A. V_{fd} and bulk doping of the HGCAL sensors

Data analysis in Figures A.15 and A.16 was realized by HGCAL Analysis Workflow software[10].

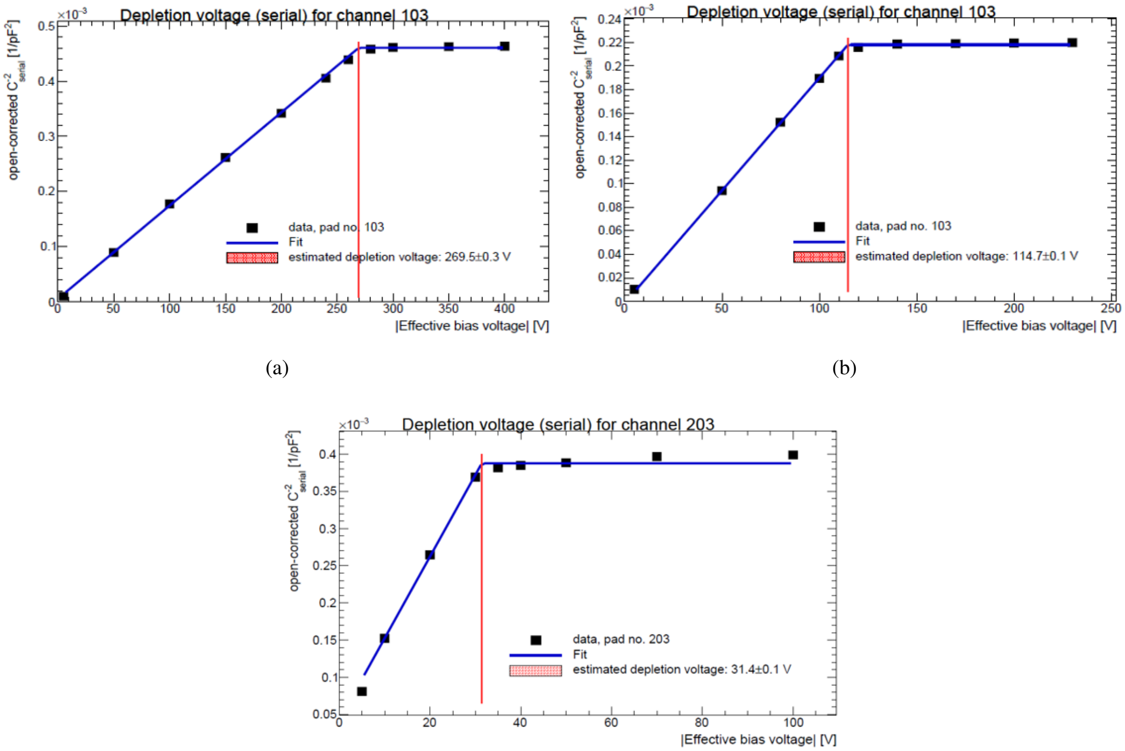

(a)

(b)

(c)

Figure A.15: Measured CV-characteristics for one representative channel in full 8-inch HGCAL sensors with oxide type ‘C’. The extracted V_{fd} is indicated at the crossing-point of the two linear fits to the dynamic- and static-regions of the $C^{-2}V$-data. (a) 300-µm-thick LD-sensor with global $\overline{V}_{\mathrm{fd}} = 255.7$ V $\pm\, 1.1\%$ and derived $\overline{N}_{\mathrm{B}} = 3.67 \times 10^{12}$ cm^{-3} $\pm\, 1.1\%$. (b) 200-µm-thick LD-sensor with global $\overline{V}_{\mathrm{fd}} = 115.7$ V $\pm\, 0.6\%$ and derived $\overline{N}_{\mathrm{B}} = 3.73 \times 10^{12}$ cm^{-3} $\pm\, 0.6\%$. (c) 120-µm-thick HD-sensor with global $\overline{V}_{\mathrm{fd}} = 31.2$ V $\pm\, 0.8\%$ and derived $\overline{N}_{\mathrm{B}} = 2.80 \times 10^{12}$ cm^{-3} $\pm\, 0.8\%$.

---

[10] https://gitlab.cern.ch/CLICdp/HGCAL/

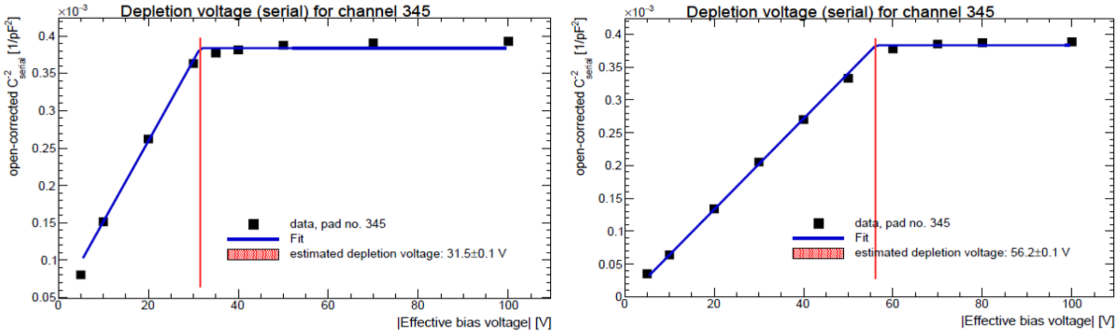

(a) (b)

Figure A.16: Measured CV-characteristics for one representative channel in 8-inch partial ('bottom-cut') 120-µm HD HGCAL sensors. (a). Sensor with oxide type 'B', and with global $\overline{V}_{\mathrm{fd}} = 31.2$ V $\pm\, 0.7\%$ and derived $\overline{N}_{\mathrm{B}} = 2.80 \times 10^{12}$ cm$^{-3} \pm 0.7\%$. (b) Sensor with oxide type 'D', and with global $\overline{V}_{\mathrm{fd}} = 55.8$ V $\pm\, 1.0\%$ and derived $\overline{N}_{\mathrm{B}} = 5.0 \times 10^{12}$ cm$^{-3} \pm 1.0\%$.